RSC Advances

PAPER

View Article Online
View Journal | View Issue

Check for updates

Cite this: *RSC Adv.*, 2017, **7**, 20062

Nitrogen-doped-carbon-coated SnO_2 nanoparticles derived from a SnO_2@MOF composite as a lithium ion battery anode material†

Fengcai Li,‡[a] Jia Du,‡[a] Hao Yang,[a] Wei Shi *[ab] and Peng Cheng *[abc]

Received 6th March 2017
Accepted 29th March 2017

DOI: 10.1039/c7ra02703f

rsc.li/rsc-advances

N-Doped-carbon-coated 2–4 nm SnO_2 nanoparticles were synthesized *via* a facile metal–organic framework (MOF) coating process followed by a calcination of the SnO_2@MOF composite. The as-prepared SnO_2 nanoparticles are well dispersed and coated with a uniform nitrogenous carbon structure, which can effectively prevent volume expansion during discharge and charge processes. Benefiting from the advantages of a synergistic effect of SnO_2 nanoparticles and carbon structure, these materials exhibit excellent electrochemical performance. For the optimized material SOC-3, a reversible specific capacity of 1032 mA h g^{-1} was maintained at 100 mA g^{-1} after 150 cycles with a coulombic efficiency of 99%. When the current was increased to 500 mA g^{-1}, a capacity of 600 mA h g^{-1} was still attained.

Open Access Article. Published on 05 April 2017. Downloaded on 1/23/2026 2:25:43 AM.
This article is licensed under a Creative Commons Attribution 3.0 Unported Licence.

Introduction

Along with the rapid development of economy and society, the energy crisis, the impending issue which restricts the progress of modern society, urgently needs to be addressed. Rechargeable lithium ion batteries (LIBs) have attracted great attention due to the remarkable superiorities of high energy density, long cycle life, excellent rate capability and environmental compatibility, which have been widely applied in cell phones, laptops and other portable devices.[1–6] The most widely used anode material for LIBs is graphite, however, its theoretical capacity is only 372 mA h g^{-1}. Searching for superior capacity and high cycling ability to substitute the traditional graphite anode material has become a research hotspot. SnO_2-based anode materials have attracted great attention because of the high theoretical capacity of 1494 mA h g^{-1}, four times higher than that of graphite.[7] Meanwhile, the high abundance, low cost and relative low charge–discharge plateau (0.6 V) also make them attractive candidates for practical use.[8,9] However, it is still quite challenging to use these materials practically because: (1) during the lithiation and delithiation processes, they may have more than 200% volume change that destroy the structure; (2) electrical conductivity is low, which reduces the electron transport; (3) during the initial lithiation process, poor initial coulombic efficiency (CE) leads to additional cathode material consumption.[7–10] There are two common methods to make up the deficiencies of SnO_2-based materials. One is to assemble active materials into different nanostructures, such as nanowires, nanofibers, nanococoons, hollow spheres and so on.[11–18] The low dimensional nanostructures can effectively accommodate the structure strain, and the large exposed surface can shorten the diffusion distance of lithium ion, which is beneficial to high rate capability. The second one is to combine carbon structure with SnO_2.[19–25] The carbon component can not only serve as a mechanical buffer for the large volume change of the active materials, but also increase the electrical conductivity of nanocomposites. The most widely used carbon components are graphite[8,13,20,23,24] and CNTs.[9,25] Usually the synthetic process of carbon coated materials is complicated and required auxiliary reagents. In order to combine carbon and active materials, some intricate methods have to be performed, such as longtime ultrasonication treatment,[8] magnetron sputtering,[19] chemical vapor deposition (CVD),[20] template method,[21] electrospinning,[22] freeze-drying.[23]

Metal–organic frameworks (MOFs) have attracted extensive research interests because of their tunable porosities and versatile functionalities,[26–28] which have been well studied for the potential applications in gas storage and separation, catalysis, sensing, gas chromatography.[29–33] Recently, by taking advantages of the thermal behaviour of MOFs, hierarchically porous carbons can be achieved.[34–38] In MOFs, well-organized carbon components from ligands can be used as sacrificial templates to prepare homogenous dispersion carbonaceous matrix or provide a carbon coating on MO nanoparticles, which is well demonstrated in LIBs.[36–42] We have taken the advantages of pore structures and adsorption properties of MOFs to explore the potential application in LIBs. For example, by carbonizing Ni-based metal–

[a]*Department of Chemistry, Key Laboratory of Advanced Energy Material Chemistry (MOE), Nankai University, Tianjin 300071, China. E-mail: shiwei@nankai.edu.cn; pcheng@nankai.edu.cn*

[b]*Collaborative Innovation Center of Chemical Science and Engineering (Tianjin), Nankai University, Tianjin 300071, China*

[c]*State Key Laboratory of Elemento-Organic Chemistry, Nankai University, Tianjin 300071, China*

† Electronic supplementary information (ESI) available. See DOI: 10.1039/c7ra02703f

‡ These authors contributed equally to this work.

This journal is © The Royal Society of Chemistry 2017

Open Access Article. Published on 05 April 2017. Downloaded on 1/23/2026 2:25:43 AM. This article is licensed under a Creative Commons Attribution 3.0 Unported Licence.

organic framework (Ni-MOF-74) with adsorptive red phosphorus precursors, NiP_2@C nanocomposites were successfully synthesized and exhibited excellent reversible capacity of 656 mA h g^{-1} at 50 mA g^{-1} after 50 cycles.[41] SnO_2@C nanocomposite exhibiting a high reversible capacity of 900 mA h g^{-1} at 100 mA g^{-1} after 50 cycles can be achieved from introducing hydrous Sn(II) ions into HKUST-1's channels followed by calcination.[42]

In this contribution, a facile and timesaving method without activation of MOFs was developed to combine MOF-derived three-dimensional hierarchical porous N-doped carbon with commercial SnO_2 nanoparticles. The final composite of SnO_2@C (SOCs) exhibits excellent performance as lithium ion batteries anode. ZIF-8, a well-known MOF, was chosen as carbon precursor since the accessible and cheap synthetic materials and simple synthetic route, as well as the N-doped carbon structures after calcination.[43–45] The highly conductive N-doped carbon constructs a three-dimensional (3D) backbone to facilitate the charge transfer. In additional, SnO_2 nanoparticles with the initial size of 50–70 nm were adhered to ZIF-8 nanoparticles accompanied by the formation of ZIF-8's structure, which greatly shorten reaction scheme. Furthermore, the size of SnO_2 nanocrystals was reduced to 2–4 nm and the nanocrystals are well coated by N-doped carbon structure after calcination, which is beneficial to prevent the large volume change and shorten lithium ion diffusion distance. The optimized SOC-3 composite achieved a reversible specific capacity of 1032 mA h g^{-1} after 150 cycles at 100 mA g^{-1}, high coulombic efficiency of 99% after 150 cycles and excellent rate performance.

Experiment

Materials preparation

All the chemicals were of analytical grade and used directly without further purification. $Zn(NO_3)_2 \cdot 6H_2O$ was purchased from Alfa, polyvinylpyrrolidone (PVP), 2-methylimidazole, SnO_2 nanoparticles were purchased from Aladdin.

Synthesis of SnO_2@ZIF-8 (SOZs). $Zn(NO_3)_2 \cdot 6H_2O$ (6 g, 20 mmol) and PVP (2 g, 0.25 mmol) were dissolved in 200 mL methanol solution, to give solution A; 2-methylimidazole (5.5 g, 57 mmol), SnO_2 (0.3 g, 2 mmol), PVP (2 g, 0.25 mmol) were dissolved in 150 mL methanol solution, to give solution B. Slowly adding solution A into solution B and then the mixture was ultrasonicated for 1 h. After washing the precipitation with 50 mL methanol twice, the product was dried at 100 °C for 12 h, to give white precipitations SnO_2@ZIF-8 (SOZ-1). Other two SOZs (SOZ-2 and SOZ-3) were synthesized following the above methods except the amounts of SnO_2 were 0.5 or 0.8 g (3.3 mmol, 5.3 mmol), respectively.

Synthesis of SnO_2@C (SOCs). The as-synthesized three SOZs were annealed in Ar atmosphere at 800 °C for 3 h. After cooling to room temperature, black composites SnO_2@C (SOC-1, SOC-2 and SOC-3) nanoparticles were obtained.

Materials characterization

Elemental analysis (EA) were measured on a PerkinElmer 2400-II CHNS analyzer. Powder X-ray diffraction (PXRD) were performed on a Rigaku Ultima IV instrument with Cu-Kα radiation ($\lambda = 1.54056$ Å), with a scan speed of 5 °C min^{-1} in the 2θ range of 3–90°. Thermo gravimetric analysis (TGA) was carried out using a NETZSCH STA 449 F3 TG-DSC analyser with a heating rate of 10 °C min^{-1} in air/Ar from room temperature to 800 °C. The morphology and microstructure were examined by scanning electron microscopy (SEM, JEOL JSM7500) and transmission electron microscopy (TEM, JEOL-2100F, 200 kV). The Raman spectrum was recorded on a Bruker RFS Raman spectrometer using laser excitation at 514.5 nm from an argon ion laser source in the range 3500–100 cm^{-1}.

Electrochemical measurements

The typical working electrode was prepared by mixing active materials with conductive materials (ketjen black) and polymer binder (poly (vinylidene fluoride) or PVDF) in a weight ratio of 8 : 1 : 1 to make slurry with 1-methyl-2-pyrrolidinone (NMP). The mixture was coated on the copper foil current collector, and then dried at 100 °C for 12 h in a vacuum oven. The coin-type cells were assembled in an argon-filled glove box with water and oxygen content below 0.1 ppm. Lithium metal served as counter and reference electrodes. 1 M $LiPF_6$ dissolving with ethylene carbonate (EC) and dimethylcarbonate (DMC) (1 : 1 in volume) was used as electrolyte with Celgard 2400 membrane as the separator. The galvanostatic charge–discharge cycling performance was measured in the potential range of 0.01–3.0 V on a LAND-CT2001A battery tester in a temperature and humidity controlled thermotank. Cyclic voltammetry (CV) tests were carried out on a PARSTAT 4000 electrochemical workstation with a scan rate of 0.1 mV s^{-1}.

Results and discussion

As illustrated in Scheme 1, the SnO_2 nanoparticles can be effectively anchored on the surface of ZIF-8 in ultrasonication synthesis process, and the final products were obtained by annealed precursors.

SEM was carried out to identify precursors' micromorphology and structures. By introducing three different proportions of the raw materials, ZIF-8 was gradually connected with increasing amounts of SnO_2 nanoparticles (Fig. S1†). PXRD was performed to verify the specific crystalline nature and phase purity of SOCs in the 2θ range of 3–90° (Fig. 1). The diffraction peaks of SOZs suggested the same crystalline structure with intensity variations, which could be indexed to SnO_2 and ZIF-8 without any impurities. The thermal behaviours of SOZs and ZIF-8 were studied using TGA in Ar atmosphere (Fig. S2†). The final products were obtained by annealing SOZs at 800 °C in a combustion boat of a tube furnace under an argon gas flow for 3 h. As for SOC-1 and SOC-2, all the PXRD peaks could be indexed to tetragonal Sn nanoparticles (JCPDS no. 4-673) and tetragonal SnO_2 nanoparticles (JCPDS no. 21-1250). The Sn nanoparticles may be classified as by-product of carbon thermal reduction SnO_2 (Fig. S3†). As shown in Fig. 2a, all PXRD peaks of SOC-3 are well in accordance with the tetragonal SnO_2 (JCPDS no. 21-1250) phase, and no diffractions from the Sn phase could

Open Access Article. Published on 05 April 2017. Downloaded on 1/23/2026 2:25:43 AM.
This article is licensed under a Creative Commons Attribution 3.0 Unported Licence.

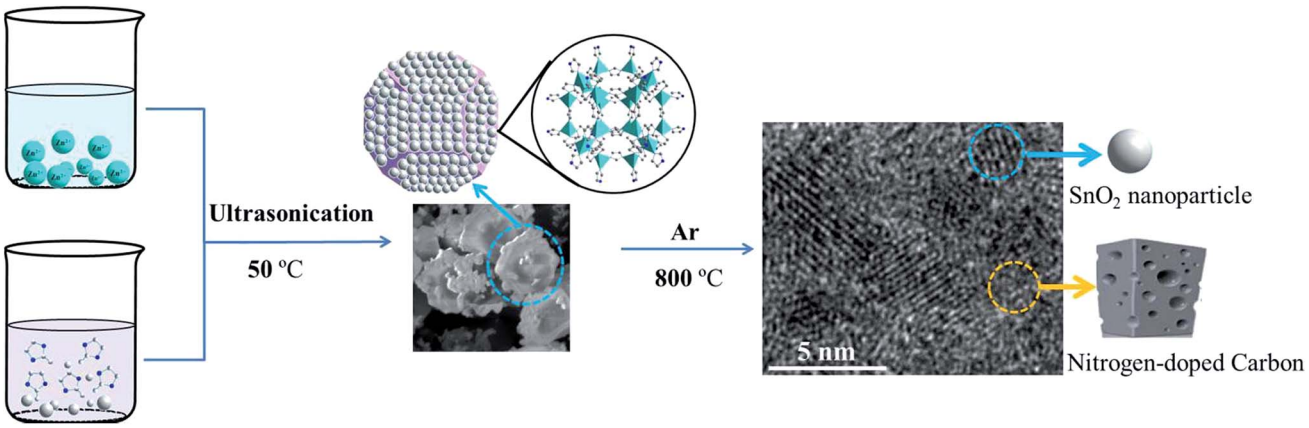

Scheme 1 Schematic illustration of the synthesis of SOCs composite.

be observed, implying the formation of a pure SnO_2 phase. The carbon structure in the SnO_2@C composite was further studied by Raman spectroscopy. For SOC-3, a lower flat peak at 1361.8 cm^{-1} and a higher sharp peak at 1580.1 cm^{-1} were observed, which can be attributed to the typical D band and G band of carbon (Fig. 2b). The G band is the result of a radial C–C stretching mode of sp^2-bonded carbon, and the G bond is from a first-order zone boundary phonon mode associated with defects in the graphene or graphene edge.[20,41,46] Because the height of the G band is higher than that of D band, this carbon material is of low defect density, which is beneficial for electron transfer. Raman peak for initial SnO_2 nanoparticles and SOC-3 were also tested to identify structural change (Fig. S4†).[47–50] The Raman spectrum change of the initial SnO_2 and SOC can also give valuable information about the particle size reduction. In initial SnO_2, the Raman peak around 633 cm^{-1} can be assigned to A_{1g} vibration, and the peak around 471 cm^{-1} is due to E_g vibration. The corresponding peaks can be observed at 616 cm^{-1} and 469 cm^{-1} in SOC-3. These peaks can confirm that SnO_2 in our materials possess the tetragonal rutile structure.[49,50] The other two materials, SOC-1 and SOC-2, also show a higher graphitization degree (Fig. S5†). The proportions of carbon and SnO_2 nanoparticles in SOCs were studied and confirmed by TGA in air atmosphere (Fig. S6†) and EA (Table S1†).

SEM was used to further examine the morphology and nanostructures of SOCs, as shown in Fig. 2c and S7.† After calcination, SOCs inherited the original morphology of SOZs. The surface of SOCs is very rough, which is beneficial to not only work as a cushion to buffer the volume change of SnO_2 nanoparticles during the charge–discharge processes, but also facilitate rapid electron transfer and provide more reaction sites during the cycling process. The carbon, tin, and nitrogen element mappings reveal the homogeneous distribution of SnO_2 nanoparticles in nitrogenous carbon structure. The combination of nitrogenous carbon skeleton and SnO_2 nanoparticles can prevent the agglomeration of SnO_2 nanoparticles generated during lithiation. HRTEM image of SOC-3 showed very small SnO_2 nanoparticles with size of 2–4 nm, surrounded by nitrogenous carbon (Fig. 2d). The well-defined lattice fringe of 0.33 nm corresponds to the (110) plane of SnO_2.

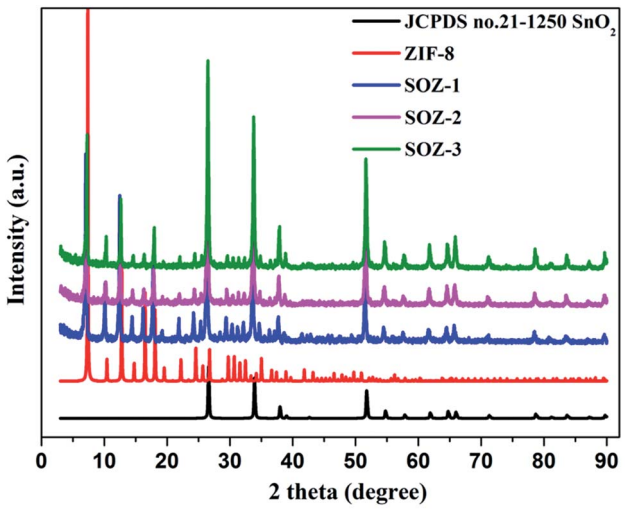

Fig. 1 PXRD of the as-prepared ZIF-8 and SOZs.

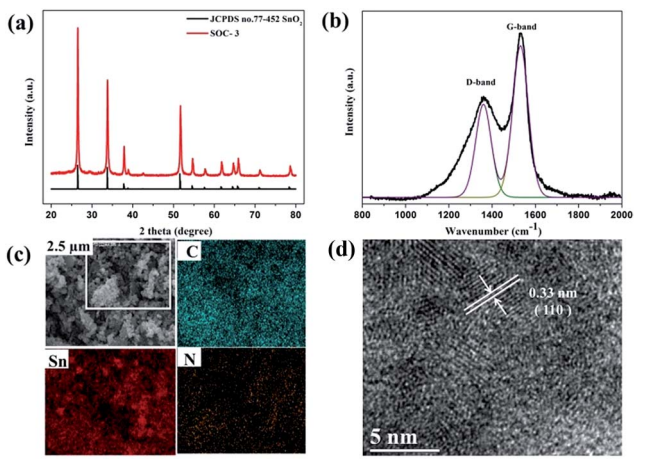

Fig. 2 PXRD (a), Raman spectrum (b), SEM image (c) and TEM image (d) of SOC-3.

This journal is © The Royal Society of Chemistry 2017

Open Access Article. Published on 05 April 2017. Downloaded on 1/23/2026 2:25:43 AM.
This article is licensed under a Creative Commons Attribution 3.0 Unported Licence.

The SOCs were studied as anode materials for LIBs. Fig. 3a–c showed discharge–charge curves of the three different materials at a current of 100 mA g^{-1} with a voltage window of 0.01–3.0 V (*vs.* Li/Li^+). SOC-1 exhibited a discharge capacity of 1390 mA h g^{-1} and a corresponding charge capacity of 910 mA h g^{-1} for the first cycle. SOC-2 showed a discharge capacity of 1270 mA h g^{-1} and a charge capacity of 885 mA h g^{-1} for the first cycle. For SOC-3, the initial discharge and charge capacities were 1650 and 1050 mA h g^{-1}, respectively, all the three materials revealed initial coulombic efficiency of less than 70%, due to the incomplete conversion involved in the formation of the solid electrolyte interphase (SEI) and the decomposition of the electrolyte.[18,51,52] From the second cycle, the coulombic efficiencies were all nearly 99%, demonstrating good reversible electrochemical property. After 150 cycles at a current of 100 mA g^{-1}, these materials exhibited steady performances of 585, 823 and 1058 mA h g^{-1} for SOC-1, SOC-2 and SOC-3, respectively (Fig. 3d). SOC-3 exhibited the best cyclic stability and the highest capacity among the three SOCs due to the high structural stability originated from the uniform distribution of SnO_2 nanoparticles in nitrogenous carbon skeleton. The SOC-3 electrode shows excellent rate performance (Fig. 3e). As the current densities vary from 50 to 100, 200, and 500 mA g^{-1}, the average specific capacities of 1050, 840, 720 and 600 mA h g^{-1} of SOC-3 can be maintained. The capacity of 806 mA h g^{-1} was regained when the current density was reduced to 50 mA g^{-1}. We have also tested its lithium storage performance at 2 A g^{-1} (Fig. S8†). And the higher current surge in 0.5 A g^{-1} for SOC-3 was lasted for 100 cycles with a capacity of 459.4 mA h g^{-1} (Fig. S9†), due to the aggregation of SnO_2 nanoparticles (100–500 nm) under the current density of 500 mA g^{-1} (Fig. S10†). The rate capabilities of the other two materials were similar and shown in Fig. S7.†

Cyclic voltammetry (CV) was used to investigate the reaction mechanism of SOC-3 between the charge and discharge cycles at a scanning rate of 0.1 mV s^{-1} in the voltage range of 0.01–3.0 V (Fig. 3f). In the first cathodic sweep process, there are two irreversible broad peaks at 0.57 and 0.75 V, due to the decomposition of SnO_2 to form Sn and the formation of a solid electrolyte interphase. Both of them were disappeared in the second cycle. The obvious peak around 0.24 V in the second cycle is due to the formation of Li–Sn alloy. The broad peak at 0.85 V corresponds to the reduction of SnO_2 to Sn and Li_2O. In the anodic sweep process, the strong peak at 0.57 V can be ascribed to the forming of Li_xSn alloy through lithium alloying with tin and broad peak at 1.24 V corresponds to Li_xSn alloy and Li_2O transforming into SnO_2. This CV behaviour is well consisted with the SnO_2-based anode materials.[7,17,20,42] The electrochemical reaction mechanism of Li with SnO_2 in lithium ion batteries can be described in the following equations:

$$4Li^+ + 4e^- + SnO_2 \leftrightarrow 2Li_2O + Sn$$

$$xLi^+ + xe^- + Sn \leftrightarrow Li_xSn\ (0 \le x \le 4.4)$$

The electrochemical impedance spectra (EIS) of SOC-3 after 100th cycling was further studied at frequencies from 100 kHz to 0.01 Hz (Fig. S11†). The charge transfer resistance (the diameter of the semicircle) decreases after 100th cycling, indicating the first several cycles are the electrode activation process and decrease the impedance value of SnO_2@C electrode, which resulted in significant improvement in the rate performance and kinetics of the reaction upon cycling.[19,41]

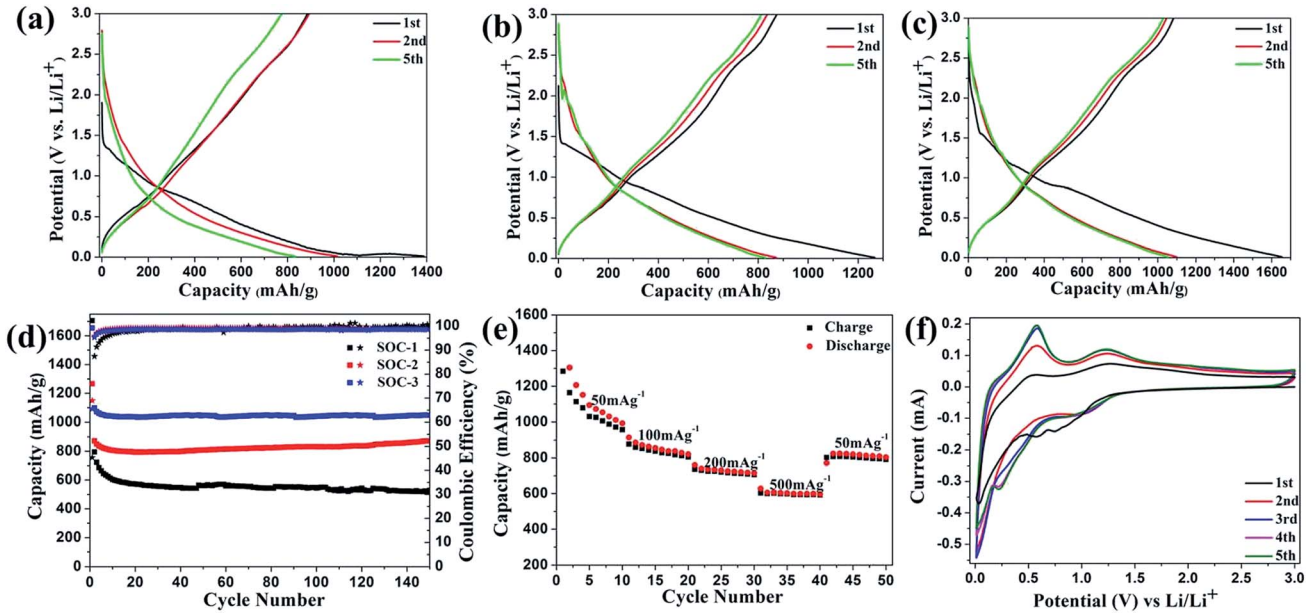

Fig. 3 Charge–discharge curves of the electrodes made of SOC-1 (a), SOC-2 (b) and SOC-3 (c) at 100 mA g^{-1}; (d) cyclic performances (□) and coulombic efficiencies (☆) of SOCs at 100 mA g^{-1} in 150 cycles; (e) rate performance of SOC-3; (f) cyclic voltammetry curves of SOC-3 at a scan rate of 0.1 mV s^{-1} in the range of 0.01–3.0 V.

Open Access Article. Published on 05 April 2017. Downloaded on 1/23/2026 2:25:43 AM. This article is licensed under a Creative Commons Attribution 3.0 Unported Licence.

In comparison with other SnO_2-based anode materials for LIBs (Table S2†), the facile synthetic route through short time ultrasonication without activation of MOFs to form SOZs and one-step pyrolysis of SOZs to form SOCs greatly shorten the reaction steps and energy cost. The synergistic effect of the 2–4 nm SnO_2 nanoparticles after calcination and the porous nitrogenous carbon structure allow our materials presents the high electrochemical performance.[42,53–68]

Conclusion

In summary, we have synthesized high performance SnO_2@C anode materials for LIBs. A straightforward strategy using unactivated metal–organic frameworks as a sacrificing template to produce nitrogenous carbon coating SnO_2 nanoparticles was demonstrated. By regulating the reaction conditions, the optimized SOC-3 exhibited a high reversible specific capacity of 1032 mA h g^{-1} after 150 cycles at 100 mA g^{-1}. The key factors governing the electrochemical performance are: (1) homogeneous dispersed SnO_2 nanoparticles can provide a high capacity and stability; (2) porous nitrogenous carbon structure derived from the ligands can effectively cushion the volume change of SnO_2 particles during lithium ion insertion–removal; (3) the calcined products of SnO_2 nanoparticles exhibit a smaller particle size than the precursor, which can shorten the diffusion length of lithium ion. Our work presents a facile method to simultaneously reduce the size of SnO_2 nanoparticles and combine SnO_2 and nitrogenous carbon together, which could be expanded to other systems of nanomaterials.

Acknowledgements

This work was supported by the National Natural Science Foundation of China (Grant numbers 21622105 and 21421001), the Ministry of Education of China (Grant numbers IRT13R30 and B12015).

References

1 B. Kang and G. Ceder, *Nature*, 2009, **458**, 190–193.
2 Z. P. Song and H. S. Zhou, *Energy Environ. Sci.*, 2013, **6**, 2280–2301.
3 N. Nitta, F. X. Wu, J. T. Lee and G. Yushin, *Mater. Today*, 2015, **18**, 252–264.
4 B. Dunn, H. Kamath and J. M. Tarascon, *Science*, 2011, **18**, 928–935.
5 P. Poizot, S. Laruelle, S. Grugeon, L. Dupont and J.-M. Tarascon, *Nature*, 2000, **407**, 496–499.
6 A. S. Aricò, P. Bruce, B. Scrosati, J.-M. Tarascon and W. V. Schalkwijk, *Nat. Mater.*, 2005, **4**, 366–377.
7 Y. Idota, T. Kubota, A. Matsufuji, Y. Maekawa and T. Miyasaka, *Science*, 1997, **276**, 1395–1397.
8 J. Lin, Z. W. Peng, C. S. Xiang, G. D. Ruan, Z. Yan, D. Natelson and J. M. Tour, *ACS Nano*, 2013, **7**, 6001–6006.
9 Z. H. Wen, Q. Wang, Q. Zhang and J. H. Li, *Adv. Funct. Mater.*, 2007, **17**, 2772–2778.
10 M. V. Reddy, G. V. Subba Rao and B. V. R. Chowdari, *Chem. Rev.*, 2013, **113**, 5364–5457.
11 P. Meduri, C. Pendyala, V. Kumar, G. U. Sumanasekera and M. K. Sunkara, *Nano Lett.*, 2009, **9**, 612–616.
12 C. Guan, X. H. Wang, Q. Zhang, Z. X. Fan, H. Zhang and H. J. Fan, *Nano Lett.*, 2014, **14**, 4852–4858.
13 L. L. Liu, M. Z. An, P. X. Yang and J. Q. Zhang, *Sci. Rep.*, 2015, **5**, 9055.
14 G. D. Park, J. K. Lee and Y. C. Kang, *Small*, 2015, **11**, 4673–4681.
15 Y. J. Hong, J.-W. Yoon, J.-H. Lee and Y. C. Kang, *Chem.–Eur. J.*, 2015, **21**, 371–376.
16 L. Li, B. Guan, L. Y. Zhang, Z. M. Su, H. M. Xie and C. G. Wang, *J. Mater. Chem. A*, 2015, **3**, 22021–22025.
17 L. Zhang, G. G. Zhang, H. B. Wu, L. Yu and X. W. Lou, *Adv. Mater.*, 2013, **25**, 2589–2593.
18 Q. N. Liu, Y. H. Dou, B. Y. Ruan, Z. Q. Sun, S. L. Chou and S. X. Dou, *Chem.–Eur. J.*, 2016, **22**, 5853–5857.
19 Y. Zhang, H. Zhang, J. Zhang, J. X. Wang and Z. C. Li, *RSC Adv.*, 2015, **5**, 106258–106264.
20 J. Qin, C. N. He, N. Q. Zhao, Z. Y. Wang, C. S. Shi, E. Z. Liu and J. J. Li, *ACS Nano*, 2014, **8**, 1728–1738.
21 X. W. Lou, C. M. Li and L. A. Archer, *Adv. Mater.*, 2009, **21**, 2536–2539.
22 X. S. Zhou, Z. H. Dai, S. H. Liu, J. C. Bao and Y. G. Guo, *Adv. Mater.*, 2014, **26**, 3943–3949.
23 X. S. Zhou, L. J. Wan and Y. G. Guo, *Adv. Mater.*, 2013, **25**, 2152–2157.
24 M. S. A. S. Shah, J. Lee, A. R. Park, Y. Choi, W.-J. Kim, J. Park, C.-H. Chung, J. Kim, B. Lim and P. J. Yooa, *Electrochim. Acta*, 2017, **224**, 201–210.
25 C. R. Ma, W. M. Zhang, Y. S. He, Q. Gong, H. Y. Che and Z. F. Ma, *Nanoscale*, 2016, **8**, 4121–4126.
26 H. C. Zhou, J. R. Long and O. M. Yaghi, *Chem. Rev.*, 2012, **112**, 673–674.
27 H. C. Zhou and S. Kitagawa, *Chem. Soc. Rev.*, 2014, **43**, 5415–5418.
28 M. O'Keeffe, *Chem. Soc. Rev.*, 2009, **38**, 1215–1217.
29 Z. J. Lin, J. Lu, M. C. Hong and R. Cao, *Chem. Soc. Rev.*, 2014, **43**, 5867–5895.
30 Q. L. Zhu and Q. Xu, *Chem. Soc. Rev.*, 2014, **43**, 5468–5512.
31 J. R. Li, J. Sculley and H. C. Zhou, *Chem. Rev.*, 2012, **112**, 869–932.
32 Y. J. Cui, Y. F. Yue, G. D. Qian and B. L. Chen, *Chem. Rev.*, 2012, **112**, 1126–1162.
33 P. Silva, S. M. F. Vilela, J. C. Tomé and F. A. A. Paz, *Chem. Soc. Rev.*, 2015, **44**, 6774–6803.
34 L. Y. Chen, J. F. Bai, C. Z. Wang, Y. Pan, M. Scheerc and X. Z. You, *Chem. Commun.*, 2008, 1581–1583.
35 P. Zhang, F. Sun, Z. H. Xiang, Z. G. Shen, J. Yun and D. P. Cao, *Energy Environ. Sci.*, 2014, **7**, 442–450.
36 J. K. Sun and Q. Xu, *Energy Environ. Sci.*, 2014, **7**, 2071–2100.
37 W. Xia, B. Qiu, D. G. Xia and R. Q. Zou, *Sci. Rep.*, 2013, **3**, 1935.
38 W. Xia, A. Mahmood, R. Q. Zou and Q. Xu, *Energy Environ. Sci.*, 2015, **8**, 1837–1866.

 This journal is © The Royal Society of Chemistry 2017

Open Access Article. Published on 05 April 2017. Downloaded on 1/23/2026 2:25:43 AM.
This article is licensed under a Creative Commons Attribution 3.0 Unported Licence.

39 S. J. Yang, S. Nam, T. Kim, J. H. Im, H. Jung, J. H. Kang, S. Wi, B. Park and C. R. Park, *J. Am. Chem. Soc.*, 2013, **135**, 7394–7397.
40 L. Zhang, H. B. Wu, S. Madhavi, H. H. Hng and X. W. Lou, *J. Am. Chem. Soc.*, 2012, **134**, 17388–17391.
41 G. H. Li, H. Yang, F. C. Li, J. Du, W. Shi and P. Cheng, *J. Mater. Chem. A*, 2016, **4**, 9593–9599.
42 M. H. Wang, H. Yang, X. L. Zhou, W. Shi, Z. Zhou and P. Cheng, *Chem. Commun.*, 2016, **52**, 717–720.
43 F. C. Zheng, Y. Yang and Q. W. Chen, *Nat. Commun.*, 2014, **5**, 5261.
44 H. B. Wang, C. J. Zhang, Z. H. Liu, L. Wang, P. X. Han, H. X. Xu, K. J. Zhang, S. M. Dong, J. H. Yao and G. L. Cui, *J. Mater. Chem.*, 2011, **21**, 5430–5434.
45 X. Wang, Q. H. Weng, X. Z. Liu, X. B. Wang, D. M. Tang, W. Tian, C. Zhang, W. Yi, D. Q. Liu, Y. Bando and D. Golberg, *Nano Lett.*, 2014, **14**, 1164–1171.
46 A. C. Ferrari and D. M. Basko, *Nat. Nanotechnol.*, 2013, **8**, 235–246.
47 S. Ding, Y. L. Liu and G. G. Siu, *Acta Phys. Sin.*, 2005, **9**, 4416–4421.
48 V. Bonu, A. Das, A. K. Sivadasan, A. K. Tyagi and S. Dhara, *J. Raman Spectrosc.*, 2015, **46**, 1037–1040.
49 H. T. Chen, X. L. Wu, Y. Y. Zhang, J. Zhu, Y. C. Cheng and P. K. Chu, *Appl. Phys. A*, 2009, **97**, 581–585.
50 S. H. Sun, G. W. Meng, G. X. Zhang, T. Gao, B. Y. Geng, L. D. Zhang and J. Zuo, *Chem. Phys. Lett.*, 2003, **376**, 103–107.
51 R. B. Wu, X. K. Qian, K. Zhou, J. Wei, J. Lou and P. M. Ajayan, *ACS Nano*, 2014, **8**, 6297–6303.
52 J. Y. Wang, N. L. Yang, H. J. Tang, Z. H. Dong, Q. Jin, M. Yang, D. Kisailus, H. J. Zhao, Z. Y. Tang and D. Wang, *Angew. Chem., Int. Ed.*, 2013, **52**, 6417–6420.
53 R. Tian, Y. Y. Zhang, Z. H. Chen, H. N. Duan, B. Y. Xu, Y. P. Guo, H. M. Kang, H. Li and H. Z. Liu, *Sci. Rep.*, 2016, **6**, 19195.
54 X. J. Zhu, Y. W. Zhu, S. Murali, M. D. Stoller and R. S. Ruoff, *J. Power Sources*, 2011, **196**, 6473–6477.
55 X. W. Lou, J. S. Chen, P. Chen and L. A. Archer, *Chem. Mater.*, 2009, **21**, 2868–2874.
56 X. F. Du, T. J. Yang, J. Lin, T. Y. Feng, J. B. Zhu, L. Lu, Y. L. Xu and J. P. Wang, *ACS Appl. Mater. Interfaces*, 2016, **8**, 15598–15606.
57 X. X. Lu, F. Yang, Y. M. Wang, X. Geng and P. Xiao, *J. Alloys Compd.*, 2015, **636**, 202–210.
58 H. Y. Mi, Y. L. Xu, W. Shi, H. Yoo, S. Park, Y. Park and S. M. Oh, *J. Mater. Chem.*, 2011, **21**, 19302–19309.
59 X. Wang, X. Q. Cao, L. Bourgeois, H. Guan, S. M. Chen, Y. T. Zhong, D. M. Tang, H. Q. Li, T. Y. Zhai, L. Li, Y. Bando and D. Golberg, *Adv. Funct. Mater.*, 2012, **22**, 2682–2690.
60 F. Ye, B. Zhao, R. Ran and Z. P. Shao, *J. Power Sources*, 2015, **290**, 61–70.
61 S. Yang, W. B. Yue, J. Zhu, Y. Ren and X. J. Yang, *Adv. Funct. Mater.*, 2013, **23**, 3570–3576.
62 J. H. Kong, W. A. Yee, L. P. Yang, Y. F. Wei, S. L. Phua, H. G. Ong, J. M. Ang, X. Li and X. H. Lu, *Chem. Commun.*, 2012, **48**, 10316–10318.
63 J. Liang, X. Y. Yu, H. Zhou, H. B. Wu, S. J. Ding and X. W. Lou, *Angew. Chem., Int. Ed.*, 2014, **53**, 12803–12807.
64 X. T. Chen, K. X. Wang, Y. B. Zhai, H. J. Zhang, X. Y. Wu, X. Wei and J. S. Chen, *Dalton Trans.*, 2014, **43**, 3137–3143.
65 Z. X. Sun, C. Cao and W. Q. Han, *RSC Adv.*, 2015, **5**, 72825–72829.
66 B. X. Wang, Z. Q. Wang, Y. J. Cui, Y. Yang, Z. Y. Wang and G. D. Qian, *RSC Adv.*, 2015, **5**, 84662–84665.
67 C. Kim, J. W. Jung, K. R. Yoon, D. Y. Youn, S. Park and I. D. Kim, *ACS Nano*, 2016, **10**, 11317–11326.
68 G. D. Park, J. K. Lee and Y. C. Kang, *Adv. Funct. Mater.*, 2017, **27**, 1603399–1603407.